Anisotropic viscosity and time-evolving lithospheric instabilities due to aligned igneous intrusions

Jonathan Perry-Houts[1] and Leif Karlstrom[1]

[1] *Department of Earth Sciences, University of Oregon, Eugene, Oregon, USA.*

1 November 2018

SUMMARY

Anisotropic viscosity is often discussed in the context of flow-induced crystallographic alignment, also known as lattice-preferred orientation, believed to exist throughout the mantle. However, other geophysical systems can produce bulk anisotropic rheology. One example is so-called shape-preferred orientation, such as that imparted by repeated, non-randomly oriented igneous intrusions. Dikes and sills tend to intrude perpendicular to least compressive tectonic stress, and therefore are typically aligned with other coeval intrusions. Intrusions provide distinct planes of weakness, producing, in a bulk sense, an anisotropic fabric to the rocks in which they are intruded. We parameterize this style of anisotropic viscosity with an effective-medium approximation, based on analytically derived characteristics of layered media. We find that the magnitude of anisotropy is highly sensitive to the presence of weak layers, even if they are relatively thin and/or sparsely distributed. We test the effects of our constitutive law on Rayleigh-Taylor instability growth, representing lithospheric instabilities. Our results indicate dramatically decreased stability of lithosphere intruded by dikes and/or sills.

Key words: Rheology: crust and lithosphere; Mechanics, theory, and modeling; Numerical modeling; Lava rheology and morphology

1 INTRODUCTION

Viscous flow is the dominant mechanism of deformation in the bulk Earth. Mechanisms that govern rheology are thus of great concern to the Earth sciences. Much work has been done to understand and quantify these mechanisms for polycrystalline rocks (e.g. Hirth & Kohlstedt 2003).

Interest has grown in understanding the presence of anisotropy in rock physics. Most work on the subject focuses on anisotropy resulting from strain-induced crystal-lattice-preferred orientation (LPO) in olivine (Hansen et al. 2016; Tommasi et al. 2009; Wendt et al. 1998) and on its relevance to mantle flow dynamics (Richter & Daly 1978; Saito & Abe 1984; Christensen 1987), lithospheric deformation of oceanic shear zones (Michibayashi & Mainprice 2004), and continental rifting (Vauchez et al. 1998).

Anisotropy also manifests on larger scales, such as that due to brittle cracks, sedimentary layering, and shear-induced melt segregation (Moore et al. 2004; Crampin 1978; Mühlhaus et al. 2002; Holtzman et al. 2003). These types of mechanisms are collectively referred to as shape-preferred orientation (SPO).

Magmatic intrusions are an example of SPO which have received little attention. Intrusions tend to form perpendicular to the orientation of least compressive stress. Therefore, coeval, proximal dikes tend to be preferentially aligned with one another. Such systems manifest on a variety of length-scales, from individual volcanic edifices to continent-scale swarms (Hou 2012).

The disparate length-scales inherently involved in these systems make modeling their dynamics difficult. Generic mechanical models exist to describe layered media (e.g. Mühlhaus et al. 2002), but no framework exists to predict anisotropic material properties in these systems. We develop an effective-medium approximation for SPO properties resulting from aligned igneous intrusions that enables the inclusion of this form of viscous anisotropy in geodynamic models.

Lithosphere may be gravitationally unstable relative to underlying mantle, owing to a combination of thermal, compositional, and tectonic effects (Houseman et al. 1981; Kay & Kay 1993). Its viscosity is therefore important in establishing long-term stability. Density-driven lithosphere removal can take many forms, but is commonly approximated by Rayleigh-Taylor instabilities (Conrad & Molnar 1997; Beall et al. 2017). Previous studies of anisotropic Rayleigh-Taylor instabilities primarily investigated analytic linear stability models, without significant analysis of time-dependence, and with intended application to lithospheric LPO (Lev & Hager 2008).

We implement our proposed rheology in the community finite element software, ASPECT (Heister et al. 2017;

Downloaded from https://academic.oup.com/gji/advance-article-abstract/doi/10.1093/gji/ggy466/5154925 by Serials Department user on 03 November 2018

Kronbichler et al. 2012; Gassmöller et al. 2016), to test its effect on long-term lithosphere dynamics. We investigate time-evolving Rayleigh-Taylor instabilities of lithosphere with a range of anisotropic parameters, representing intrusive volcanic systems. Our models demonstrate the significance of igneous intrusions on lithosphere stability, as well as the importance of time-dependence in modeling lithosphere dynamics.

2 GOVERNING EQUATIONS

We consider deformations for which momentum balance is well-approximated by low-Reynolds number, gravity-driven flow,

$$\tau_{ij,j} - p\delta_{ij} + \rho g_i = 0, \tag{1}$$

with deviatoric stress, τ_{ij}; density, ρ; gravity, g_i; pressure, p; and the Kronecker delta, δ_{ij}. Commas in subscripts denote spatial derivatives with respect to the following index. Flow must also satisfy the mass-balance continuity equation

$$(\rho u_i)_{,i} = 0 \tag{2}$$

where u_i is velocity.

Additionally, we track compositional fields which advect with velocity u_i,

$$\dot{c}_x + u_i c_{x,i} = q_x, \tag{3}$$

with a distinct source term, q_x, for each field, c_x, and overdot representing a derivative with respect to time.

Linear rheology is described by a fourth-order constitutive tensor, C_{ijkl}, which maps strain rate to deviatoric stress without loss of generality,

$$\tau_{ij} = 2C_{ijkl}\dot{\varepsilon}_{kl}, \tag{4}$$

where $\dot{\varepsilon}_{ij} = \frac{1}{2}[u_{i,j} + u_{j,i}]$ is the strain rate.

One of the simplest forms of anisotropy is called transverse isotropy (TI), defined by a single anomalous plane (Saito & Abe 1984; Honda 1986; Mühlhaus et al. 2002). Building on Saito & Abe (1984), Honda (1986) showed that a TI rheology may be parameterized by two scalars– a normal viscosity (η_N), and a shear viscosity (η_S), activated in pure shear, and simple shear with respect to the orientation of the material fabric, respectively. This constitutive behavior implicitly depends on the orientation of anisotropy, which we denote using a vector, n_i, normal to the material fabric. Pure and simple shear are defined relative to n_i such that

$$\dot{\varepsilon}_{ij}n_i = \begin{cases} \dot{\varepsilon}_{11}n_1 + \dot{\varepsilon}_{22}n_2 & \text{in pure shear,} \\ \dot{\varepsilon}_{21}n_1 + \dot{\varepsilon}_{12}n_2 & \text{in simple shear.} \end{cases} \tag{5}$$

Following Mühlhaus et al. (2002), we employ a TI constitutive law that modifies the standard viscosity along a single plane,

$$\tau_{ij} = 2\eta_N\dot{\varepsilon}_{ij} - 2(\eta_N - \eta_S)\Lambda_{ijkl}\dot{\varepsilon}_{kl}, \tag{6}$$

where Λ is a fourth-order tensor that imparts orientation-dependence, relative to n_i,

$$\Lambda_{ijkl} = \frac{1}{2}(n_i n_k \delta_{lj} + n_j n_k \delta_{il} + n_i n_l \delta_{kj} + n_j n_l \delta_{ik}) - 2n_i n_j n_k n_l. \tag{7}$$

The director orientation, n_i, varies in time as a function of the deformation gradient,

$$\dot{n}_i = [u_{i,j} - \dot{\varepsilon}_{ij} - \dot{\varepsilon}_{ki}n_k n_j + \dot{\varepsilon}_{kj}n_k n_i]\, n_j. \tag{8}$$

Because energy is not dissipated under solid-body rotation, the constitutive equation (6) deals only with the symmetric part of the velocity gradient. As a result, C_{ijkl} must also be symmetric. For a fourth-order tensor that means $C_{ijkl} = C_{jikl} = C_{ijlk} = C_{jilk}$. Therefore, the material model is insensitive to differences between orthogonal senses of the same simple shear.

Entropy also requires that C_{ijkl} be positive definite, that is, the material must dissipate a positive amount of energy under any deformation. Therefore, the full constitutive law must also be insensitive to differences between pure shear which is normal or parallel to n_i. Thus, we make no distinction between materials with orthogonal planes of anisotropy. The most distinct fabric orientations are then oriented 45° relative to one another (i.e. $n_i^A n_i^B = \sqrt{2}/2$, for materials, A, and B). In the following sections we compare models with horizontal, and 45° dipping fabrics, following the approach of Lev & Hager (2008).

3 EFFECTIVE-MEDIUM APPROXIMATION

In order to prescribe values for η_N and η_S, we need to understand the bulk effect of material layering. Kendall & Silver (1998) define an effective-medium for TI seismic anisotropy, based on the model of Tandon & Weng (1984) that assumes oblate inclusions of distinct material properties. Because dikes and sills are large, continuous features, they more closely approximate the limiting case of large-aspect-ratio inclusions, or laminate layering (Backus 1962). This assumption allows us to solve analytically for exact values of shear and normal viscosity as functions of individual layer properties.

We begin by defining a representative volume element (RVE) which spans a typical, 'statistically homogeneous,' volume of the real material (Christensen 2005). For the case of igneous intrusions, the natural RVE is a column of rock whose height, h, encompasses a cycle from one intrusion to the next; i.e. a layered stack which contains a dike or sill, and a layer of host rock (Fig. 1A). We assume that layer-parallel deformation is uniform, which reduces our RVE to a 1-dimensional profile of length h. We retain the volume element terminology for consistency with other work.

In defining an effective-medium, we aim to find a homogeneous fluid that behaves comparably over h as the RVE does (Hashin 1983). We formulate our homogenization in terms of power flux,

$$\int_0^h \eta^e \dot{\varepsilon}^e_{ij}\dot{\varepsilon}^e_{ij} dz = \int_0^h \eta \dot{\varepsilon}_{ij}\dot{\varepsilon}_{ij} dz, \tag{9}$$

with RVE viscosity, η; effective viscosity, η^e; and strain rate fields within the RVE and effective models, $\dot{\varepsilon}$, and $\dot{\varepsilon}^e$, respectively.

Downloaded from https://academic.oup.com/gji/advance-article-abstract/doi/10.1093/gji/ggy466/5154925 by Serials Department user on 03 November 2018

3.1 Normal viscosity

Under pure shear, strain rate within the RVE is uniform, and equation (9) reduces to

$$h\eta_N^e = \int_0^h \eta(z)dz, \tag{10}$$

for effective normal viscosity, η_N^e.

In the discretized, N-layer case, equation (10) can be written as the weighted arithmetic mean of the RVE constituent viscosities,

$$\eta_N^e = \frac{\Sigma_{i=1}^N \eta_i h_i}{\Sigma_{i=1}^N h_i}, \tag{11}$$

where η_i and h_i are viscosity and thickness of layer i, respectively.

3.2 Shear viscosity

In simple shear, the strain rate field within the same RVE is non-uniform because weak layers can accommodate more strain than strong layers.

To find a homogeneous effective shear viscosity, we first simplify equation (9) by noting that strain rate must be continuous. Therefore, stress must be constant throughout both the RVE and effective column, reducing equation (9) to

$$\int_0^h \tau_{ij}\dot{\varepsilon}_{ij}^e dz = \int_0^h \tau_{ij}\dot{\varepsilon}_{ij} dz. \tag{12}$$

By inverting the linear, isotropic constitutive law of the individual layers, we get

$$\dot{\varepsilon}_{ij} = \frac{\tau_{ij}}{\eta}, \tag{13}$$

and equation (12) further reduces to

$$\frac{h}{\eta^e} = \int_0^h \frac{1}{\eta} dz. \tag{14}$$

Similar to our derivation of equation (11), for the case of a discretized medium, equation (14) can be written

$$\eta_S^e = \frac{\Sigma_{i=1}^N h_i}{\Sigma_{i=1}^N \frac{h_i}{\eta_i}}. \tag{15}$$

That is, the weighted harmonic mean of the RVE's constituent viscosities.

Equation (15) shows that shear viscosity is highly sensitive to the viscosity of the weakest layer, and insensitive to the relative layer thicknesses, suggesting that, for example, a sparse distribution of molten sills can reduce the effective shear viscosity of its host to near that of liquid magma (Fig. 1). In comparison, equation (11) is highly sensitive to the presence of strong layers, and insensitive to the properties of weak layers. Therefore, a weak host rock dissected by solidified sills, for example, may become substantially stronger under normal shear than it was without the intrusions. The difference between the two viscosities defines the system's magnitude of anisotropy, and suggests that SPO can have profound effects. Here we define anisotropy magnitude as $1 - \eta_S/\eta_N$, such that the magnitude is zero for isotropic materials, and asymptotically approaches 1 as the ratio of shear to normal viscosity decreases.

For example, the Mesoproterozoic Mackenzie igneous events occurred within a very short duration, erupting over $650,000$ km^3 of basalt through a 2400 km $\times$ 1800 km dike swarm exposed in the northern Canadian Shield (Gittings 2008). The region averages one 30 meter thick dike per 72 kilometers across strike (LeCheminant & Heaman 1989). Assuming an average dike viscosity of approximately 10^3 Pa$\cdot$s during emplacement, and an average host viscosity approximately 10^{23} Pa$\cdot$s, we expect an effective shear viscosity, $\eta_S^e \approx 2.5 \times 10^6$ Pa$\cdot$s, and normal viscosity, $\eta_N^e \approx 9.9 \times 10^{22}$ Pa$\cdot$s. This represents a shear viscosity reduction of almost 17 orders of magnitude, substantially higher than that from olivine LPO, which produces approximately one order of magnitude in shear viscosity reduction (Hansen et al. 2012, 2016).

3.3 Limitations

We make several significant assumptions in this effective medium formulation that deserve further discussion.

First, we assume that magmatic intrusions have infinite planar extent. This assumption holds so long as anisotropic model cells have at least one continuous through-going intrusion, and discontinuous intrusions are separated by a resolvable distance. It does not hold for intrusions smaller than discretization scale, or rocks with very widely spaced intrusions where the composite cannot be considered statistically homogeneous.

Second, we assume that buckling instabilities do not develop with wavelengths smaller than discretization. In such a case, layer-parallel simple shear along the weak layers will begin to accommodate strain under macroscopic pure shear (Schmalholz & Podladchikov 2001). This scenario violates the assumption in Section 3.1 that strain rate is uniform under pure shear. Effective normal viscosity in this case will decrease, reducing the net magnitude of anisotropy.

Systems for which our assumptions do not hold may still exhibit viscous anisotropy, and therefore may be analyzed in the context of our parameter space search (Sec. 4.2; Fig. 3), but the effective medium developed here does not directly apply. We argue that our model is a good fit for large dike swarms, such as those emplaced during flood basalt eruptions, where dikes can be hundreds of kilometers long, and tens of meters thick.

4 GEODYNAMIC MODELS

We have shown that the presence of mechanically distinct layers, such as those produced by igneous intrusions, significantly modifies the bulk rheology of the host rock (Sec. 3; Fig. 1). Following Lev & Hager (2008), we hypothesize that this will affect lithospheric instabilities in volcanically-active regions.

To test our hypothesis, we solve equations (1)–(8), (11), and (15) with ASPECT version `2.0.0-pre` (Bangerth et al. 2017). We run a Monte Carlo ensemble of unstably-stratified models with various anisotropic and geometric parameters to analyze the effect of viscous anisotropy on long-term growth properties of Rayleigh-Taylor instabilities. All code and documentation required to reproduce these results is included in the supplement to this paper.

Downloaded from https://academic.oup.com/gji/advance-article-abstract/doi/10.1093/gji/ggy466/5154925 by Serials Department user on 03 November 2018

4.1 Model setup

Each model in our ensemble has two-dimensional Cartesian geometry with variable width, w, depth, d, and a thin, anisotropic, dense upper domain, underlain by a buoyant, isotropic lower domain, identified by index, X, in model property subscripts (Fig. 2). Velocity is fixed (no-slip) on the top, reflecting (free-slip) on the sides, and unconstrained (stress-free) on the bottom.

Model properties are nondimensionalized, following the scaling of Lev & Hager (2008). Total depth is constant, $d = 1$, in all models. The upper domain has density $\rho_1 = 1$, with mean thickness, $d_1 = 0.15$. The lower domain has density $\rho_2 = 0$, and thickness, $d_2 = 0.85$. The model is accelerated by a downward gravitational constant, $g = (0, -1.0)$.

Normal viscosity is constant throughout the model, $\eta_N = 1e-3$. The upper layer has an initially-uniform anisotropic fabric which is oriented either horizontally (0°), or diagonally (45°), with variable shear viscosity. The lower layer is isotropic in all models, $\eta_S = \eta_N$. The orientation of anisotropy through time obeys equation (8), but the magnitude is assumed to remain constant within each fluid.

The fluid interface is vertically perturbed by a sinusoidal function of lateral distance, with amplitude 0.01, and wavelength equal to the model width $\lambda = w$. Wave number is interpreted as a function of the model width, $k = 2\pi/w$. The interface is smoothed in depth to minimize discretization-dependent effects on long-term convective behavior (Bangerth et al. 2017),

$$X = \frac{1}{2}\left[3 + \tanh\left(\frac{z - d_2 - 0.01\cos(2\pi x/w)}{0.005}\right)\right], \quad (16)$$

in Cartesian coordinates, x, and z.

Model width, and thus wavenumber, is varied among the ensemble in order to simulate non-integer wavenumbers using finite-width model domains. We discuss this approach in more detail in Appendix A2.2.

Each model is adaptively refined up to resolution equivalent of 1024×1024 mesh cells (cell geometry ≈ 0.001 high by $w/1025$ wide) near the fluid interface, and as low as 16×16 equivalent elsewhere. Mesh refinement is adjusted every 10 model steps to ensure continuous resolution of the fluid interface. Time step lengths are adaptive, satisfying a Courant number, 1.0. Models are terminated when the fluid interface reaches 45% of the model depth. We vary anisotropy magnitude in the upper layer, $0 \leq 1 - \eta_S/\eta_N \leq 0.95$, and model width, $0.2 \leq w \leq 5$. More information on the numerical implementation is included in Appendix A.

4.2 Analysis

Because the time progression of instability depends strongly on effective viscosity, we compare models at equal interface displacements, rather than equal times. That is, we compare snapshots of models taken when the interface perturbation has grown to a particular amplitude, rather than comparing snapshots taken at equal model times. This helps normalize results among models with very different effective viscosities, where one model may have terminated before another has even begun to move significantly.

From each model snapshot, we query both total time elapsed, t, and maximum vertical interface velocity, taken to be the model's instantaneous growth rate, as functions of interface displacement. Model time discretization means that we don't necessarily have snapshots of all models when their fluid interface is displaced by any given amount. By interpolating to a common set of displacement snapshots we can directly compare the progression of instability growth among models (Fig. 3).

At each displacement snapshot, we fit a polynomial to growth rate for the entire ensemble. This helps smooth spatial and temporal discretization differences between models, especially significant at low displacement amplitudes. Because the results are best visualized in log space with respect to wave-number and growth rate, we fit a function to the logarithm of both quantities,

$$\log(G) = \Gamma_1 \log(k)^2 + \Gamma_2 \log(k) + \Gamma_3, \quad (17)$$

for growth rate, G, with coefficients, Γ_i, as linear functions of anisotropy magnitude in the horizontal and dipping bases,

$$\Gamma_i = \alpha_i H + \beta_i D + \gamma_i \quad (18)$$

where α_i, β_i, and γ_i are fit parameters; H and D are magnitudes of horizontal and dipping anisotropy, respectively:

$$H = \begin{cases} 1.0 - \eta_S/\eta_N & \text{if } \theta = 0°, \\ 0 & \text{otherwise,} \end{cases} \quad (19)$$

and

$$D = \begin{cases} 1.0 - \eta_S/\eta_N & \text{if } \theta = 45°, \\ 0 & \text{otherwise,} \end{cases} \quad (20)$$

where θ is the model's initial anisotropic fabric orientation, relative to horizontal.

We interpret the most unstable wavenumber, k_{max}, as the wavenumber where instantaneous growth rate is highest,

$$\left.\frac{\partial G}{\partial k}\right|_{k_{max}} = 0, \quad (21)$$

$$k_{max} = -\frac{\alpha_2 H + \beta_2 D + \gamma_2}{\alpha_1 H + \beta_1 D + \gamma_1}. \quad (22)$$

Both growth rate, and k_{max} are shown in Fig. 3, projected into the H ($D = 0$), and D ($H = 0$) planes.

4.3 Results

Analytic solutions of Lev & Hager (2008) suggest that lithosphere with dipping anisotropy is more unstable than that with horizontal anisotropy. Our results show that this is only true in the early stages of model development, and does not hold for time-evolving systems (Fig. 4). In fact, models with initially-horizontal anisotropic fabric significantly out-pace models with dipping initial fabric relatively quickly.

Further, Lev & Hager (2008) find that horizontal anisotropy generates substantially longer wavelength drips than that with dipping anisotropy in the instantaneous limit, $t \to 0$. We show that this result also cannot be trivially extrapolated to long-term convective behavior. Models with either orientation of initial anisotropy tend to converge over time, becoming more closely aligned with values of the initially-horizontal models.

Downloaded from https://academic.oup.com/gji/advance-article-abstract/doi/10.1093/gji/ggy466/5154925 by Serials Department user on 03 November 2018

The rate and dominant wavelength with which instabilities develop in anisotropic models, regardless of their initial orientation, is substantially different than models with isotropic fabric. The existence of anisotropy in any form is much more consequential to potential gravitational instabilities than its orientation.

5 DISCUSSION

Elkins-Tanton & Hager (2000) showed that magmatic intrusions may induce lower-crustal instabilities by crystallizing dense mineral phases. Subsequently, intrusion-triggered delamination has been invoked to explain enigmatic observations from continental magmatic episodes globally, including the Siberian Traps of northern Russia (Elkins-Tanton 2005), the southern Rocky Mountain ignimbrite flare-up of the Cordilleran U.S. (Farmer et al. 2008), the Columbia River flood basalts of the northwestern U.S. (Hales et al. 2005; Camp & Hanan 2008), and the Songliao basin of northeastern China (Wang et al. 2006). This hypothesis is consistent with geophysical and geochemical observations that are otherwise difficult to reconcile.

The same study found that the ability of such a mechanism to produce gravity-driven instabilities relies on the existence of a weak layer on which dense lower-crust can detach from the buoyant upper-crust (Elkins-Tanton & Hager 2000), consistent with conclusions drawn from many delamination modeling efforts (Elkins-Tanton 2005; Burov et al. 2007; Krystopowicz & Currie 2013; Beall et al. 2017). Our results support the conclusion that lithospheric delamination requires weakened regions, but suggest an alternative interpretation for their origin. We have shown that molten intrusions can soften the host rock to nearly the viscosity of liquid magma, along certain planes of weakness. Therefore, we suggest that magmatic intrusions themselves may provide the low viscosity layers necessary for efficient lithospheric delamination. This proposed mechanism connects the apparent necessity of mechanically weak layers with prior work on intrusion-delamination-eruption feedbacks.

It should be noted that our lithospheric foundering models assume that fractures extend to the base of the lithosphere. While smooth, continuous fractures are common in the crust, magma transport in the mantle lithosphere is typically more complex (e.g. Holtzman et al. 2003; Keller & Katz 2016). However, we take the observation from flood basalt eruptions, that episodes of very high magma flux can rapidly transport large volumes of melt across the lithosphere, to suggest that lithosphere-scale dikes are a plausible mechanism of magma transport during such atypical events.

Our models also assume that anisotropy magnitude remains constant through time, but the systems we aim to model are dynamic, and material properties evolve with time. In particular, heat transport between host rock and intrusion can modify the viscosity of both, changing the overall magnitude of anisotropy. Heat transfer during pervasive intrusion emplacement causes profound weakening of the host rock (Karlstrom & Richards 2011; Karlstrom et al. 2017; Dufek & Bergantz 2005). Conversely, over longer intervals, intrusions become more viscous as they cool and solidify, potentially even surpassing the host rock's viscosity. In such cases, the system's anisotropy parameters can change drastically through time, but the model's kinematics will still fall within the parameter space mapped in Fig.3. Understanding the lithosphere's thermodynamic state through the course of a magmatic episode will be an important future direction of this work.

6 SUMMARY

We have demonstrated that magmatic intrusions can produce strong anisotropic fabric in rock to which they are emplaced. The magnitude of resulting anisotropy is highly sensitive to the ratio of intrusion viscosity to host rock viscosity. In magmatic systems, this effect may produce anisotropic fabric many orders of magnitude stronger than that generated by other mechanisms.

Dense lithosphere, with even modest reduction in shear viscosity, forms Rayleigh-Taylor instabilities on much shorter timescales than equivalent isotropic lithosphere. Our results suggest that volcanically active regions may be inherently more prone to lithospheric delamination than other areas. This finding is consistent with other studies suggesting that continental volcanism is often associated with delamination events. Thus, we propose that weakening produced by magmatic intrusions may contribute to the rapid acceleration of volcanism seen in many large igneous provinces.

APPENDIX A: NUMERICAL IMPLEMENTATION

A1 Equations

To enable anisotropic viscosity in ASPECT, we substitute the scalar viscosity, η, with a symmetric fourth-order tensor, C_{ijkl}, representing an arbitrary linear map from strain rate to deviatoric stress. The full momentum balance equation solved by ASPECT is extended to

$$2\left(C_{ijkl}\dot{\varepsilon}_{kl} - \frac{1}{3}(C_{iikl}\dot{\varepsilon}_{kl}\delta_{ij})\right)_{,j} - p\delta_{ij} + \rho g_i = 0. \quad \text{(A.1)}$$

We modify the viscous heating term in ASPECT's thermal advection-diffusion equation accordingly,

$$\rho C_p\left(T_{,t} + u_i T_{,i}\right) - \left(\rho C_p \kappa T_{,i}\right)_{,i} = \ldots$$
$$+2\left(C_{ijkl}\dot{\varepsilon}_{kl} - \frac{1}{3}(C_{iikl}\dot{\varepsilon}_{kl}\delta_{ij})\right) : \left(\dot{\varepsilon}_{ij} - \frac{1}{3}u_{i,i}\delta_{ij}\right) + \ldots \quad \text{(A.2)}$$

The full equations are more general than the scope of this work. Specifically, in the models presented above, we assume the fluid is incompressible, and we do not consider temperature diffusion. The extra terms are shown here, and included in the supplementary code, for completeness.

We track spatially variable quantities with $dim + 3$ additional fields that advect with the fluid velocity, where dim is the model's spatial dimension. All of the models in this paper are 2-dimensional ($dim = 2$), but the model can be trivially extended to 3-D.

ASPECT is agnostic to the purpose of the compositional fields, and only modifies them while solving equation (3). Our code is implemented as a plug-in to ASPECT that

Downloaded from https://academic.oup.com/gji/advance-article-abstract/doi/10.1093/gji/ggy466/5154925 by Serials Department user on 03 November 2018

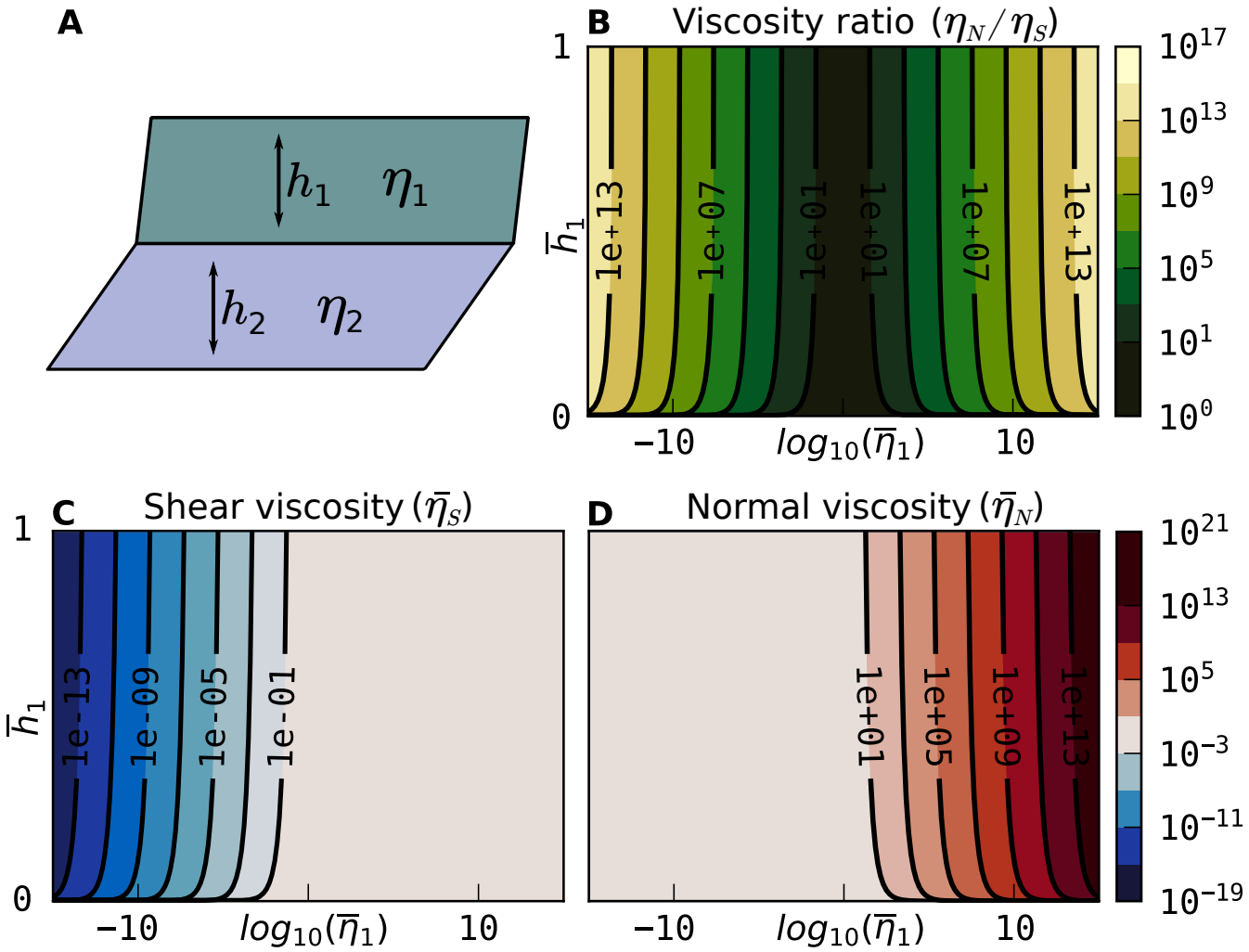

Figure 1. Effective viscosity of a periodic, two-layer medium as a function of layer viscosity and thickness ratios. Axes are shared between sub-figures **B-D**. Variables with overbars are normalized to the equivalent property in layer 2. **A**: Schematic representation of a layered medium, representing a dike-host rock cycle. **B**: Ratio of shear to normal viscosity, demonstrating that anisotropy magnitude is highly sensitive to the viscosity ratio, and insensitive to relative thickness of the layers. **C-D**: Shear viscosity and normal viscosity on same axes as **B**, demonstrating that simple-shear deformation is primarily sensitive to properties of the weaker layer, while normal viscosity is more sensitive to the stronger layer.

interprets these fields as: model domain, X; shear viscosity, η_S; normal viscosity, η_N; and n_i, the *dim* components of director vector, respectively. It returns coefficients for the governing equations:

$$C_{ijkl} = \eta_N \mathbf{1} - (\eta_N - \eta_S)\Lambda_{ijkl}, \tag{A.3}$$

with fourth-order identity tensor, $\mathbf{1}$, director tensor Λ, as defined in equation (7); density,

$$\rho = \begin{cases} 1 & \text{if } X = 1, \\ 0 & \text{if } X = 2; \end{cases} \tag{A.4}$$

and source/sink terms for equation (3), which simulate the time-dependent variation of n_i, via equation (8),

$$q_i = \dot{n}_i. \tag{A.5}$$

A2 Validation

We perform several validations of our implementation.

A2.1 Method of manufactured solutions

First, we verify that we are accurately solving the governing equations by testing convergence to a manufactured solution (Roy 2005).

Beginning with known velocity solution,

$$u = (\sin(2y)\sin(2x), (\cos(2y) + 1)\cos(2x)), \tag{A.6}$$

and constitutive tensor, C_{ijkl}, representing a uniform anisotropic fluid, we manually solve equation (1) for ρg_i. Equation (A.6) was chosen because it isolates simple shear, and pure shear within the same model domain.

We impose the derived body force in an identical ASPECT model, and invert for velocity, expecting our solution to equal the known solution (Eq. A.6). Pressure is constrained to zero everywhere, in order to isolate the velocity components of our solution. We compute the model error as the difference between the numerical solution, and the analytic one in the L_1 and L_2 norms, as a function of mesh size,

Downloaded from https://academic.oup.com/gji/advance-article-abstract/doi/10.1093/gji/ggy466/5154925 by Serials Department user on 03 November 2018

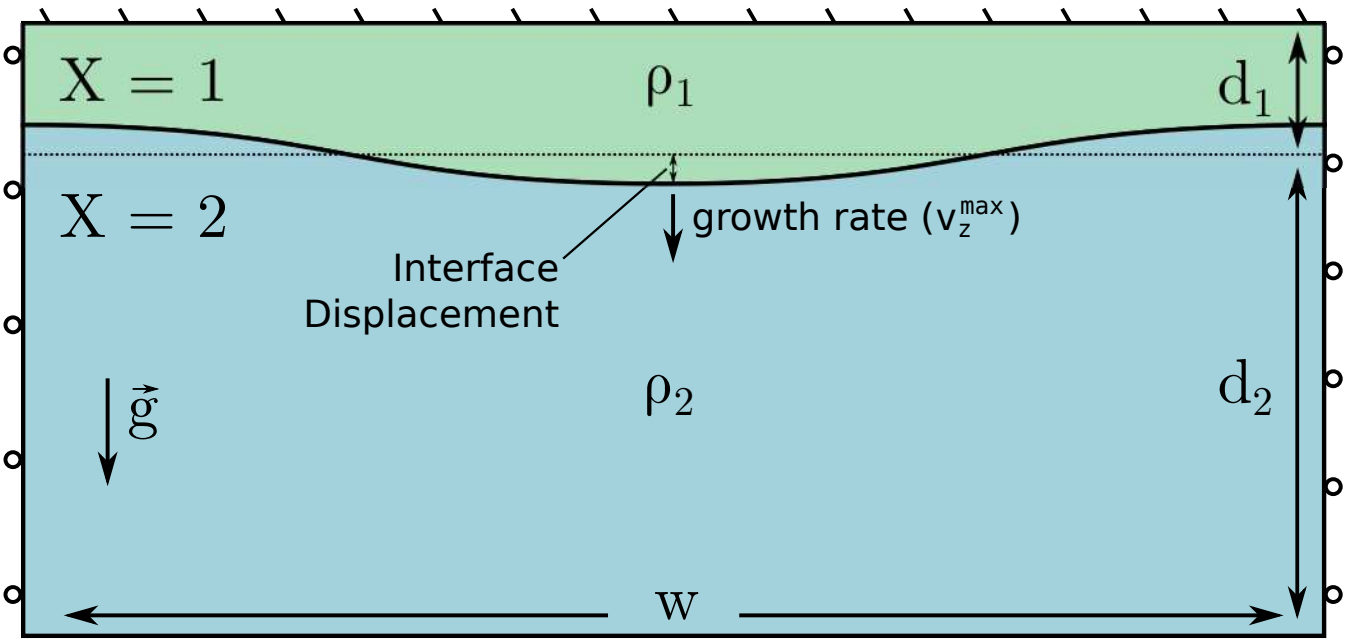

Figure 2. Gravitationally unstable model setup with a dense, anisotropic upper layer. We analyze an ensemble of models with various perturbation wavelengths and anisotropy parameters, to investigate Rayleigh-Taylor instabilities in lithosphere modified by aligned igneous intrusions. Model properties are described in the text.

h. Our implementation converges with the expected order, $\mathcal{O}(h^3)$ (Kronbichler et al. 2012), in both norms (Fig. A1).

A2.2 Rayleigh-Taylor growth

We further validate our model against the analytic solutions of Lev & Hager (2008). The model setup is identical to that described in Section 4.1, where the anisotropic models have magnitude 0.9. We solve equations (1) and (2), once for each model. In each case, we interpret the average vertical velocity along the fluid interface as the instability growth rate. Our solutions align well with analytic solutions (Fig. A2).

We tested several approaches to reproduce these solutions. Our initial attempts were based on a single model for each anisotropy orientation, in which we perturbed the fluid interface by many frequencies, and attempted to measure the growth rate and dominant frequency. This method proved difficult both because of numerical discretization limitations which make superimposed perturbations difficult to resolve, and the constraint that finite-width model domains can only contain integer wavenumbers, which limits generality of the solutions. Further, the maximum instability wavenumber, k_{max}, becomes difficult to define over finite-time, where the interface undergoes significant deformation, which would make this test less relevant to our finite-time models, discussed in the main text.

Our results are substantially closer to the analytic solution than those of Lev & Hager (2008), possibly owing to the specifics of our model setup. In particular, the method described above, of perturbing the interface with a single frequency per model, and varying the model width across many runs, seemed to result in the single most significant improvement over other methods we tried.

ACKNOWLEDGMENTS

We thank Lars Hansen and James Hammond for constructive reviews that improved the quality and clarity of this paper. We also thank the developers and contributors to the ASPECT project, as well as the Computational Infrastructure for Geodynamics (geodynamics.org), which is funded by National Science Foundation grants EAR-0949446 and EAR-1550901, for supporting ASPECT's development. This work was supported by National Science Foundation grant EAR-1727451.

Downloaded from https://academic.oup.com/gji/advance-article-abstract/doi/10.1093/gji/ggy466/5154925 by Serials Department user on 03 November 2018

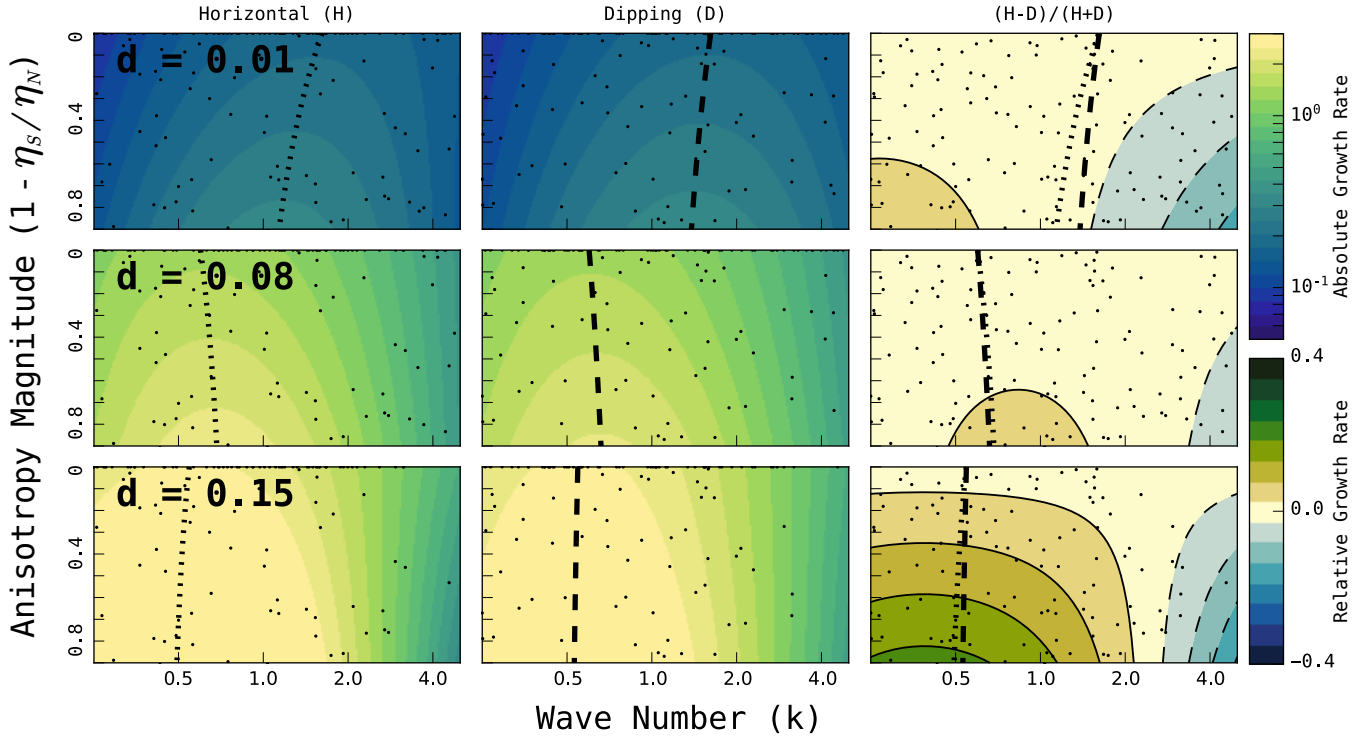

Figure 3. Snapshots of instability growth rate through model time. We sample instability growth rates from an ensemble of anisotropic Rayleigh-Taylor models (black dots) when each one reaches specified fluid interface displacement distances, $\mathbf{d} = \{0.01, 0.08, 0.15\}$ (subplot rows). Each model has an anisotropic, dense, upper layer, with either horizontal (H), or dipping (D) initial fabric (Fig. 2), fixed anisotropy magnitude, $1-\eta_S/\eta_N$, and fixed wavenumber, k. We fit a parabolic surface to the ensemble's modeled growth rate in each snapshot, as a function of wavenumber and anisotropy magnitude. Best fit surfaces for the horizontal models and dipping models are shown in the left, and middle columns, respectively, with warmer colors representing faster instability growth. The normalized difference between horizontal and dipping models is plotted in the right column, where areas of parameter space where horizontally anisotropic models outpace dipping models are shown in green, and vice versa in blue. The most unstable wavenumber, as a function of anisotropy magnitude, is plotted with a dotted line for the horizontal models, and a dashed line for the dipping models. Both lines are overlain on the third column for direct comparison. Adjusted R^2 values for the parabolic fits are, from top to bottom: 0.80, 0.93, and 0.97. While all models have similar initial growth rates, with dipping models slightly faster than horizontal, initially horizontal models ultimately out-pace the others, demonstrating that instantaneous linear stability analysis of anisotropic Rayleigh-Taylor dynamics cannot be assumed to apply to time-dependent problems.

Downloaded from https://academic.oup.com/gji/advance-article-abstract/doi/10.1093/gji/ggy466/5154925 by Serials Department user on 03 November 2018

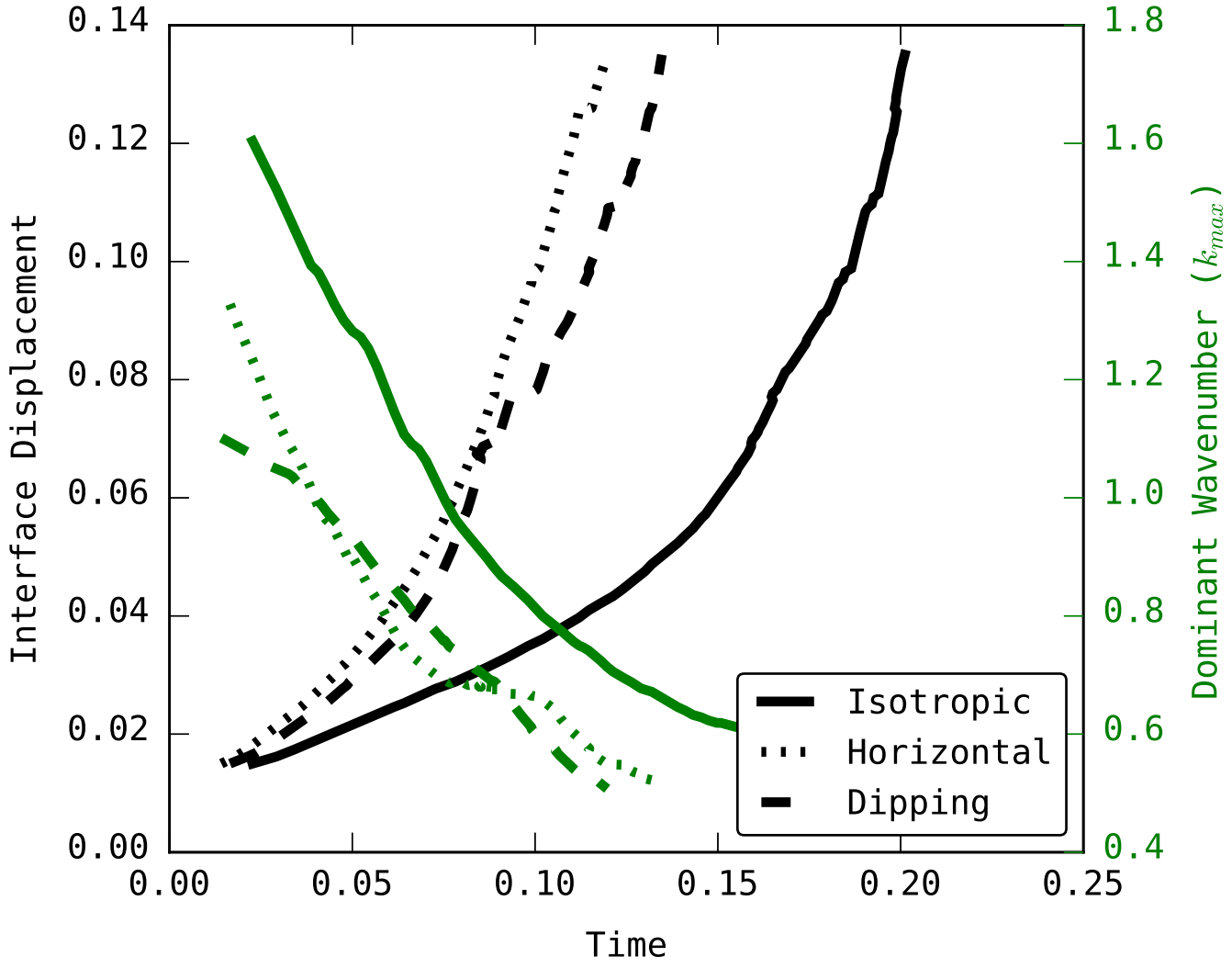

Figure 4. Interface displacement of Rayleigh-Taylor instabilities with horizontal, dipping, and isotropic initial fabrics. Horizontal and dipping models have anisotropy magnitude, $1 - \eta_S/\eta_N = 0.9$ in the dense upper layer. The isotropic model has constant viscosity, $\eta_S = \eta_N$. All models demonstrate exponential growth during early stages, followed by super-exponential growth over longer time scales, as is expected for Rayleigh-Taylor instability growth.

Downloaded from https://academic.oup.com/gji/advance-article-abstract/doi/10.1093/gji/ggy466/5154925 by Serials Department user on 03 November 2018

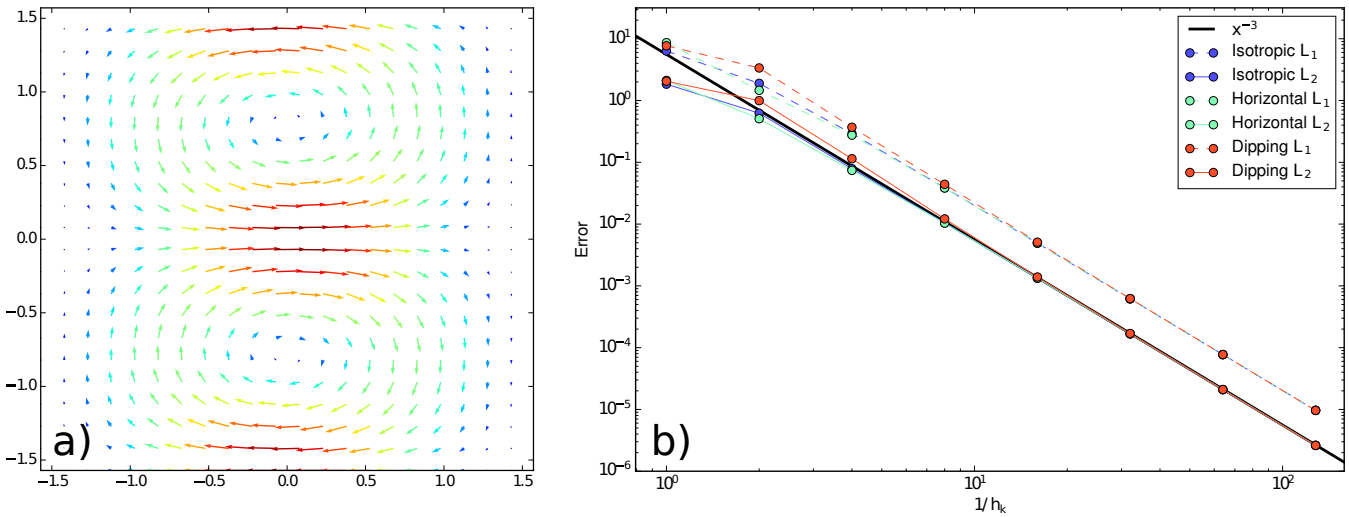

Figure A1. Convergence to a manufactured solution demonstrates expected accuracy of finite element solver. **A**: Analytically defined velocity field, chosen to isolate both pure shear and simple shear. **B**: Reduction of model error relative to analytic solution as a function of mesh cell size, h, in both L_1 and L_2 norms.

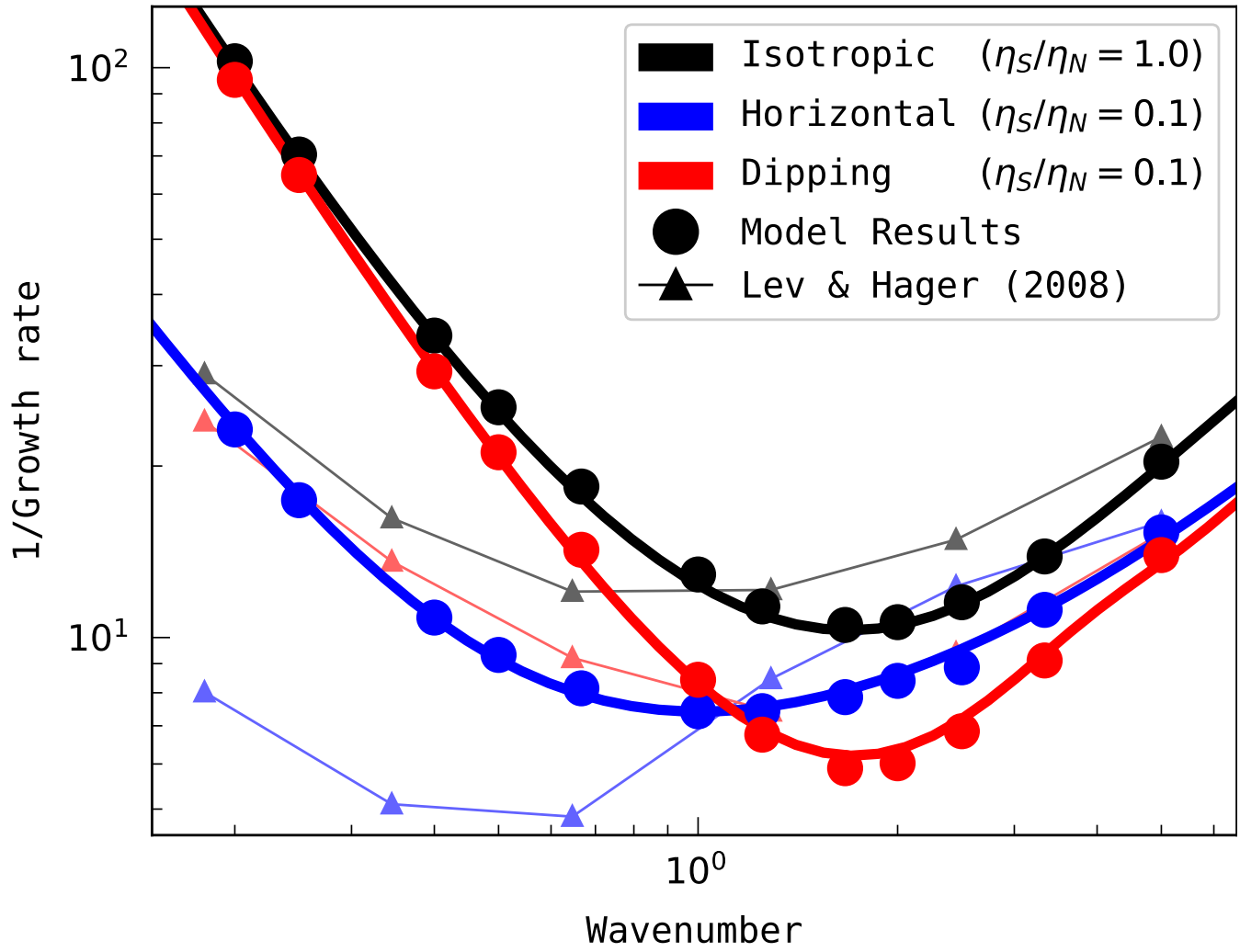

Figure A2. Rayleigh-Taylor instability growth rates from our numerical models (dots) compare well with analytic solutions of Lev & Hager (2008) (thick lines). Our solutions show a significant model fit improvement over previous numerical implementations (triangles), especially at low wavenumbers.

Downloaded from https://academic.oup.com/gji/advance-article-abstract/doi/10.1093/gji/ggy466/5154925 by Serials Department user on 03 November 2018

REFERENCES

Backus, G. E., 1962. Long-wave elastic anisotropy produced by horizontal layering, *Journal of Geophysical Research*, **67**(11), 4427–4440.

Bangerth, W., Dannberg, J., Gassmöller, R., Heister, T., & others, 2017. ASPECT: Advanced Solver for Problems in Earth's ConvecTion, User manual.

Beall, A. P., Moresi, L., & Stern, T., 2017. Dripping or delamination? A range of mechanisms for removing the lower crust or lithosphere, *Geophys J Int*.

Burov, E., Guillou-Frottier, L., d'Acremont, E., Le Pourhiet, L., & Cloetingh, S., 2007. Plume head–lithosphere interactions near intra-continental plate boundaries, *Tectonophysics*, **434**(1), 15–38.

Camp, V. E. & Hanan, B. B., 2008. A plume-triggered delamination origin for the Columbia River Basalt Group, *Geosphere*, **4**(3), 480–495.

Christensen, R. M., 2005. *Mechanics of Composite Materials*, Dover Civil and Mechanical Engineering, Dover Publications.

Christensen, U. R., 1987. Some geodynamical effects of anisotropic viscosity, *Geophys. J. R. Astron. Soc.*, **91**(3), 711–736.

Conrad, C. P. & Molnar, P., 1997. The growth of Rayleigh–Taylor-type instabilities in the lithosphere for various rheological and density structures, *Geophys. J. Int.*, **129**(1), 95–112.

Crampin, S., 1978. Seismic-wave propagation through a cracked solid: Polarization as a possible dilatancy diagnostic, *Geophys J Int*, **53**(3), 467–496.

Dufek, J. & Bergantz, G. W., 2005. Lower crustal magma genesis and preservation: A stochastic framework for the evaluation of basalt–crust interaction, *J Petrology*, **46**(11), 2167–2195.

Elkins-Tanton, L. T., 2005. Continental magmatism caused by lithospheric delamination, *Geological Society of America Special Papers*, **388**, 449–461.

Elkins-Tanton, L. T. & Hager, B. H., 2000. Melt intrusion as a trigger for lithospheric foundering and the eruption of the Siberian flood basalts, *Geophysical Research Letters*, **27**(23), 3937–3940.

Farmer, G. L., Bailley, T., & Elkins-Tanton, L. T., 2008. Mantle source volumes and the origin of the mid-Tertiary ignimbrite flare-up in the southern Rocky Mountains, western U.S., *Lithos*, **102**(1–2), 279–294.

Gassmöller, R., Heien, E., Puckett, E. G., & Bangerth, W., 2016. Flexible and scalable particle-in-cell methods for massively parallel computations, *ArXiv161203369 Phys.*.

Gittings, F. W., 2008. Geological report on the Muskox Property, Tech. Rep. NTS 86 O/6, Platinex Inc., Coppermine River Area, Nunavut.

Hales, T. C., Abt, D. L., Humphreys, E. D., & Roering, J. J., 2005. A lithospheric instability origin for Columbia River flood basalts and Wallowa Mountains uplift in northeast Oregon, *Nature*, **438**(7069), 842–845.

Hansen, L. N., Zimmerman, M. E., & Kohlstedt, D. L., 2012. Laboratory measurements of the viscous anisotropy of olivine aggregates, *Nature*, **492**(7429), 415–418.

Hansen, L. N., Warren, J. M., Zimmerman, M. E., & Kohlstedt, D. L., 2016. Viscous anisotropy of textured olivine aggregates, part 1: Measurement of the magnitude and evolution of anisotropy, *Earth Planet. Sci. Lett.*, **445**, 92–103.

Hashin, Z., 1983. Analysis of composite materials—a survey, *Journal of Applied Mechanics*, **50**(3), 481–505.

Heister, T., Dannberg, J., Gassmöller, R., & Bangerth, W., 2017. High accuracy mantle convection simulation through modern numerical methods – II: Realistic models and problems, *Geophys J Int*, **210**(2), 833–851.

Hirth, G. & Kohlstedt, D., 2003. Rheology of the upper mantle and the mantle wedge: A view from the experimentalists, in *Inside the Subduction Factory*, vol. 138 of **Geophysical Monograph Series**, pp. 83–105, ed. Eiler, J., American Geophysical Union.

Holtzman, B. K., Kohlstedt, D. L., Zimmerman, M. E., Heidelbach, F., Hiraga, T., & Hustoft, J., 2003. Melt segregation and strain partitioning: Implications for seismic anisotropy and mantle flow, *Science*, **301**(5637), 1227–1230.

Honda, S., 1986. Strong anisotropic flow in a finely layered asthenosphere, *Geophys. Res. Lett.*, **13**(13), 1454–1457.

Hou, G., 2012. Mechanism for three types of mafic dyke swarms, *Geoscience Frontiers*, **3**(2), 217–223.

Houseman, G. A., McKenzie, D. P., & Molnar, P., 1981. Convective instability of a thickened boundary layer and its relevance for the thermal evolution of continental convergent belts, *Journal of Geophysical Research: Solid Earth*, **86**(B7), 6115–6132.

Karlstrom, L. & Richards, M., 2011. On the evolution of large ultramafic magma chambers and timescales for flood basalt eruptions, *J. Geophys. Res.*, **116**(B8), B08216.

Karlstrom, L., Paterson, S. R., & Jellinek, A. M., 2017. A reverse energy cascade for crustal magma transport, *Nat. Geosci.*, **10**(8), 604–608.

Kay, R. & Kay, S., 1993. Delamination and delamination magmatism, *Tectonophysics*, **219**(1-3), 177–189.

Keller, T. & Katz, R. F., 2016. The role of volatiles in reactive melt transport in the asthenosphere, *J. Petrol.*, **57**(6), 1073–1108.

Kendall, J.-M. & Silver, P. G., 1998. Investigating causes of D″ anistropy, *Core-Mantle Bound. Reg.*.

Kronbichler, M., Heister, T., & Bangerth, W., 2012. High accuracy mantle convection simulation through modern numerical methods, *Geophys. J. Int.*, **191**(1), 12–29.

Krystopowicz, N. J. & Currie, C. A., 2013. Crustal eclogitization and lithosphere delamination in orogens, *Earth and Planetary Science Letters*, **361**, 195–207.

LeCheminant, A. N. & Heaman, L. M., 1989. Mackenzie igneous events, Canada: Middle Proterozoic hotspot magmatism associated with ocean opening, *Earth and Planetary Science Letters*, **96**(1), 38–48.

Lev, E. & Hager, B. H., 2008. Rayleigh–Taylor instabilities with anisotropic lithospheric viscosity, *Geophys. J. Int.*, **173**(3), 806–814.

Michibayashi, K. & Mainprice, D., 2004. The role of preexisting mechanical anisotropy on shear zone development within oceanic mantle lithosphere: An example from the Oman ophiolite, *J Petrology*, **45**(2), 405–414.

Moore, M. M., Garnero, E. J., Lay, T., & Williams, Q., 2004. Shear wave splitting and waveform complexity for lowermost mantle structures with low-velocity lamellae and transverse isotropy, *Journal of Geophysical Research: Solid Earth*, **109**(B2).

Mühlhaus, H.-B., Moresi, L., Hobbs, B., & Dufour, F., 2002. Large amplitude folding in finely layered viscoelastic rock structures, *Pure appl. geophys.*, **159**(10), 2311–2333.

Richter, F. M. & Daly, S. F., 1978. Convection models having a multiplicity of large horizontal scales, *J. Geophys. Res.*, **83**(B10), 4951–4956.

Roy, C. J., 2005. Review of code and solution verification procedures for computational simulation, *Journal of Computational Physics*, **205**(1), 131–156.

Saito, M. & Abe, Y., 1984. Consequences of anisotropic viscosity in the Earth's mantle, *Zisin J. Seismol. Soc. Jpn. 2nd Ser*, **37**(2), 237–245.

Schmalholz, S. M. & Podladchikov, Y. Y., 2001. Strain and competence contrast estimation from fold shape, *Tectonophysics*, **340**(3), 195–213.

Tandon, G. P. & Weng, G. J., 1984. The effect of aspect ratio of inclusions on the elastic properties of unidirectionally aligned composites, *Polymer Composites*, **5**(4), 327–333.

Tommasi, A., Knoll, M., Vauchez, A., Signorelli, J. W., Thoraval, C., & Logé, R., 2009. Structural reactivation in plate

Downloaded from https://academic.oup.com/gji/advance-article-abstract/doi/10.1093/gji/ggy466/5154925 by Serials Department user on 03 November 2018

tectonics controlled by olivine crystal anisotropy, *Nat. Geosci.*, **2**(6), 423–427.

Vauchez, A., Tommasi, A., & Barruol, G., 1998. Rheological heterogeneity, mechanical anisotropy and deformation of the continental lithosphere, *Tectonophysics*, **296**(1), 61–86.

Wang, F., Zhou, X.-H., Zhang, L.-C., Ying, J.-F., Zhang, Y.-T., Wu, F.-Y., & Zhu, R.-X., 2006. Late Mesozoic volcanism in the Great Xing'an Range (NE China): Timing and implications for the dynamic setting of NE Asia, *Earth Planet. Sci. Lett.*, **251**(1-2), 179–198.

Wendt, A. S., Mainprice, D., Rutter, E., & Wirth, R., 1998. A joint study of experimental deformation and experimentally induced microstructures of pretextured peridotites, *J. Geophys. Res.*, **103**(B8), 18205–18221.

Downloaded from https://academic.oup.com/gji/advance-article-abstract/doi/10.1093/gji/ggy466/5154925 by Serials Department user on 03 November 2018